



Magnetic bond-order potential for iron-cobalt alloys

Aleksei Egorov ¹, Aparna P. A. Subramanyam,¹ Ziyi Yuan,² Ralf Drautz ¹ and Thomas Hammerschmidt ¹

¹ICAMS, Ruhr-Universität Bochum, Universitätsstrasse 150, 44780 Bochum, Germany

²Department of Materials, University of Oxford, Parks Road, Oxford OX1 3PH, United Kingdom



(Received 26 August 2022; accepted 14 March 2023; published 10 April 2023)

For large-scale atomistic simulations of magnetic materials, the interplay of atomic and magnetic degrees of freedom needs to be described with high computational efficiency. Here we present an analytic bond-order potential (BOP) for iron-cobalt, an interatomic potential based on a coarse-grained description of the electronic structure. We fitted BOP parameters to magnetic and non-magnetic density functional theory (DFT) calculations of Fe, Co, and Fe-Co bulk phases. Our BOP captures the electronic structure of magnetic and nonmagnetic Fe-Co phases. It provides accurate predictions of structural stability, elastic constants, phonons, point and planar defects, and structural transformations. It also reproduces the DFT-predicted sequence of stable ordered phases peculiar to Fe-Co and the stabilization of B2 against disordered phases by magnetism. Our Fe-Co BOP is suitable for atomistic simulations with thousands and millions of atoms.

DOI: [10.1103/PhysRevMaterials.7.044403](https://doi.org/10.1103/PhysRevMaterials.7.044403)

I. INTRODUCTION

Fe-Co is a magnetic alloy with the highest saturation magnetization among all materials [1,2], which places it at the top of the Slater-Pauling curve [3,4]. Together with high permeability and high Curie temperature, Fe-Co alloys are suitable for high-performance transformers, solenoid valves, magnetostrictive transducers, and other uses [5].

Fe-Co alloys tend to order, so the B2 (CsCl) phase, where Co atoms are at the corners of the bcc conventional unit cell and Fe at the center, forms below 1000 K at 1:1 composition [6,7]. Above this temperature, the alloy transforms to disordered bcc. Abrikosov *et al.* [8], using density functional theory (DFT), revealed that at 0 K, ordered and partially ordered ferromagnetic B2 are the most stable phase from 0 to 85 at. % Co. Neumayer and Fähnle [9] addressed the role of magnetism for the ordering in light of structural defects. They found that Fe and Co antisite defects in the B2 phase have small but positive formation energies for magnetic DFT calculations. Positive formation energy prevents the spontaneous exchange of Fe and Co atoms and transformation to disordered bcc. For the nonmagnetic case, antisite defects also have small but negative formation energies, making B2 unstable compared to disordered bcc. Thus magnetism is crucial for structural stability in Fe-Co.

Large-scale atomistic simulations of magnetic alloys such as Fe-Co are still challenging. Modeling and simulation of lattice defects like dislocations, grain boundaries, or cracks often require cell sizes from a few thousand to hundreds of thousands of atoms [10–15]. DFT provides high accuracy but is limited to only a few hundred atoms. Simulations with many atoms are possible with empirical interatomic potentials, but they usually do not capture the electronic structure and magnetism. For this reason, for example, empirical potentials are unreliable in simulations of dislocations in bcc transition metals [16,17] and, consequently, their alloys, including Fe-Co. Machine learning potentials combine high precision and

computational efficiency but require a vast amount of reference DFT data [18–21]. Besides, incorporating magnetism is still tricky, and the first magnetic machine learning potentials are just appearing [22–24]. Thus accurate electronic structure methods with lower computational costs than DFT are necessary for simulations of magnetic transition-metal alloys.

Analytic bond-order potentials (BOPs) are an electronic structure method derived from quantum mechanics with an explicit treatment of magnetism [25,26]. Analytic BOPs and the underlying tight-binding bond model have shown their applicability to nonmagnetic transition metals, such as Ta, W, Nb, Mo [27], and Ti [28], as well as the magnetic transition metals Mn [29] and Fe [30–32]. BOP was also successfully used to study iron's magnetic [33] and structural [34] phase transitions at finite temperatures. At the same time, analytic BOPs are efficient enough for simulations with millions of atoms [35,36].

In this work we present an analytic BOP for Fe-Co alloys. We discuss in detail the parametrization procedure, including reference data, fitting process, and validation strategies. We further validate the BOP by comparing central material properties such as energy-volume curves, phonons, the electronic density of states, defect formation energies, and elastic constants with DFT and experimental data. We further compute the convex hull of Fe-Co across the whole composition range and find that it contains a dense sequence of ordered, stable phases in excellent agreement with DFT calculations.

II. ANALYTIC BOND-ORDER POTENTIALS

Analytic bond-order potentials are interatomic potentials derived from quantum mechanics by a two-step coarse graining from DFT to a tight-binding (TB) bond model [37] and from TB to BOPs [26,38]. The BOPs transparently describe the interatomic interactions and scale linearly with the system size [39]. As a result, BOPs allow simulations of systems with millions of atoms [35,36].

The total binding energy of the BOP is given as

$$E_{\text{tot}} = E_{\text{bond}} + E_{\text{emb}} + E_{\text{mag}} + E_{\text{rep}}, \quad (1)$$

with the bond energy E_{bond} , the embedding energy E_{emb} , the magnetic energy E_{mag} , and the repulsive energy E_{rep} , just as in the TB bond model.

The bond energy E_{bond} results from the formation of chemical bonds of the atom-centered orbitals of neighboring atoms. It is determined by integrating the local density of states (DOS) $n_{I\alpha,s}$ up to the Fermi energy E_F ,

$$E_{\text{bond}} = \sum_{I\alpha,s} \int^{E_F} (E - E_{I\alpha}) n_{I\alpha,s}(E) dE, \quad (2)$$

of orbitals α of atom I with onsite levels $E_{I\alpha}$ and s is either spin-up or spin-down. The onsite levels $E_{I\alpha}$ are obtained in a self-consistency loop that minimizes the total energy E_{tot} with respect to $E_{I\alpha}$ (see Ref. [39] for details). In TB, the DOS is computed by diagonalization of the system-wide Hamiltonian \hat{H} , while in analytic BOP, from the moments of the local DOS,

$$\mu_{I\alpha}^{(p)} = \int E^p n_{I\alpha}(E) dE, \quad (3)$$

for the nonmagnetic case, where $\mu_{I\alpha}^{(p)}$ is the p th moment of the DOS of orbital α of atom I . We can also compute moments from all self-returning hopping paths of length p that start and end at $|I\alpha\rangle$ as

$$\begin{aligned} \mu_{I\alpha}^{(p)} &= \langle I\alpha | \hat{H}^p | I\alpha \rangle \\ &= \sum_{J\beta K\gamma \dots} \langle I\alpha | \hat{H} | J\beta \rangle \langle J\beta | \hat{H} | K\gamma \rangle \langle K\gamma | \hat{H} | \dots \rangle \dots \langle \dots | \hat{H} | I\alpha \rangle \\ &= \sum_{J\beta K\gamma \dots} H_{I\alpha J\beta} H_{J\beta K\gamma} H_{K\gamma \dots} \dots H_{\dots I\alpha}, \end{aligned} \quad (4)$$

with the Hamiltonian matrix elements $H_{I\alpha J\beta}$ between pairs of orbitals α and β on atoms I and J . For the magnetic case, we need to evaluate moments in Eqs. (3) and (4) separately for spin-up and spin-down and then sum them up (see Ref. [26] for details). Nondiagonal matrix elements $H_{I\alpha J\beta}$ in Eq. (4), also known as hopping or bond integrals, are distance dependent. We can represent them in the parameterized form [Eq. (5)] to later fit parameters to reference data, as discussed in Sec. III. The equality of Eqs. (3) and (4) directly relates the electronic structure (DOS) to the atomic structure (self-returning hopping paths). It is a core feature of the BOP methodology [40].

Higher moments [with a higher value of p in Eq. (3)] correspond to longer hopping paths and hence a more far-sighted exploration of the local atomic environment. Four moments are sufficient to distinguish fcc and bcc structures in transition metals [41]. Six moments are needed to capture the trend of structural stability hcp \rightarrow bcc \rightarrow hcp \rightarrow fcc across the 4d and 5d transition-metal series [25]. In the limit of an infinite number of moments, we would recover the TB solution. For our Fe-Co BOP, we used nine moments as in an existing BOP for iron [32] that showed that nine moments are an appropriate trade-off between computational efficiency and accuracy. We employed the Jackson kernel with 200 extended moments to smoothen the truncation of the BOP expansion with a constant terminator as described in Refs. [39,42]. The analytic

BOP calculations in this work are performed with the BOPfox software package [39].

The setup of the pairwise Hamiltonian $H_{I\alpha J\beta}$ for TB/BOP calculations depends on the system. Both s and d electrons in Fe and Co contribute to bond formation. We approximate the interatomic interaction with an orthogonal, d -valent Hamiltonian in a two-center approximation. Cawkwell *et al.* showed that neglecting sp and sd interactions is an excellent approximation for iridium [43]; therefore, it is justified for Fe-Co with similar band filling. The resulting 5×5 Hamiltonian of two interacting d -valent atoms I and J at a distance R contains three independent bond integrals $dd\sigma$, $dd\pi$, and $dd\delta$, which we represent as a sum of exponential functions

$$\beta(R) = \sum_{k=1}^{k_{\text{max}}} c_k \exp(-\lambda_k R^{n_k}), \quad (5)$$

where c_k , λ_k , and n_k are the parameters to fit. This simple functional form has been used successfully for the bond integrals obtained from projecting the DFT eigenstates onto an orthogonal TB basis [44]. For Fe-Co BOP, we found that three exponentials ($k_{\text{max}} = 3$) for the $dd\sigma$ bond and two ($k_{\text{max}} = 2$) for $dd\pi$ and $dd\delta$ provide a numerically robust optimization and sufficient flexibility to reach the target precision.

Omitting the s electrons is compensated by the embedding energy E_{emb} in Eq. (1). Following the second-moment approximation of TB, where the cohesive energy of an atom i scales as the square root of the densities of the surrounding atoms, we express the embedding energy as

$$E_{\text{emb}} = - \sum_i \sqrt{\sum_{j \neq i} \rho(r_{ij})}, \quad (6)$$

where the electron density $\rho(r_{ij})$ is represented as

$$\rho(r_{ij}) = p_1 \exp[-p_2(r_{ij} - p_3)^2], \quad (7)$$

with the parameters p_1 , p_2 , and p_3 to be optimized.

The magnetic energy in Eq. (1) is given by the Stoner model for ferromagnetism [45],

$$E_{\text{mag}} = -\frac{1}{4} \sum_i I_i m_i^2, \quad (8)$$

where I_i is the Stoner exchange integral on atom i . The magnetic moment on atom i is the difference in the number of spin-up and spin-down electrons, $m_i = N_i^\uparrow - N_i^\downarrow$, after the self-consistent solution is obtained [see description of Eq. (2)].

The repulsive energy in Eq. (1) has two main components in our model. The first is a pairwise repulsion with the same functional form as the binding energy [Eq. (5)]. In particular, we used one exponential [$k_{\text{max}} = 1$ in Eq. (5)] for all interactions (Fe-Fe, Co-Co, and Fe-Co), which is sufficient for the pairwise repulsion as shown in previous parametrizations. The second component of the repulsive energy for our model is a short-range core repulsion of the form

$$E_{\text{core}}(r_{ij}) = p_2(p_1 - r_{ij})^3 / r_{ij} \exp(p_1 - r_{ij}), \quad (9)$$

where r_{ij} is the distance between atoms i and j . The parameters p_1 and p_2 are set to 1.5 and 100, respectively, to ensure

that the atoms are strongly repulsive at a distance shorter than 1.5 Å.

For reproducing the elastic constant C_{44} for elemental Fe, we also used an environment-dependent Yukawa repulsion for Fe-Fe interactions:

$$E_{\text{Yuk}} = \frac{1}{2} \sum_{i,j} \frac{B}{r_{ij}} \exp[-\lambda_{ij}(r_{ij} - 2r_{\text{core}})], \quad (10)$$

where

$$\lambda_{ij} = \frac{1}{2}(\lambda_i + \lambda_j), \quad (11)$$

and

$$\lambda_i = \lambda_0 + \left[\sum_{l \neq i} C \exp(-\nu r_{il}) \right]^{1/m}, \quad (12)$$

where B , r_{core} , λ_0 , C , ν and m are parameters to fit; r_{ij} and r_{il} are the separations between atoms i and j , or i and l , respectively. Znam *et al.* [46] successfully used environment-dependent repulsion of this form in TiAl BOP to reproduce Cauchy pressures.

The interaction range of the BOP is limited to r_c by cutoff functions:

$$f(r) = \begin{cases} 1 & \text{if } r < (r_c - d_c), \\ 0 & \text{if } r > r_c, \\ \frac{1}{2}(\cos\langle\pi[\frac{r-(r_c-d_c)}{d_c}]\rangle + 1) & \text{else,} \end{cases} \quad (13)$$

that act on the bond integrals, embedding energy, and repulsive energy. d_c is the length over which these terms go from their value at $r = r_c - d_c$ to zero at $r = r_c$.

III. PARAMETERIZATION

A. Reference data

We fitted the Fe-Co BOP to DFT reference data. The physical model underlying the analytic BOPs allows us to work with small reference data sets. For the Fe-Fe and Co-Co interactions, we used as a reference the energy-volume (E-V) curves of ferromagnetic (FM) and nonmagnetic (NM) bcc, fcc, and hcp structures which appear in the Fe-Co phase diagram [47]. For the Fe-Fe interaction, we also included several sheared structures of FM bcc to get a better value of the elastic constant C_{44} of elemental Fe. For the Fe-Co interaction, we used the E-V curves of FM B2 (CsCl) as the most stable phase at 1:1 composition at low temperatures and NM B2 to cover the energy difference between FM and NM structures. We also included an FM B32 (NaTi), which is slightly higher in energy than B2, and the bcc-based ordered L6₀-Fe₃Co (Ti₃Cu) as the most stable Fe₃Co structure according to DFT (with marginally lower energy than D0₃) [48,49]. The DFT E-V curves that were used to parametrize the Fe-Co interaction are shown in Fig. 4.

We performed DFT calculations using the VASP software package [50–52] with the projector augmented wave method (PAW) for pseudopotentials [53] and the PBE (Perdew-Burke-Ernzerhof) [54] exchange-correlation functional. We used dense Monkhorst-Pack k -point meshes [55] and 400 eV as energy cutoff.

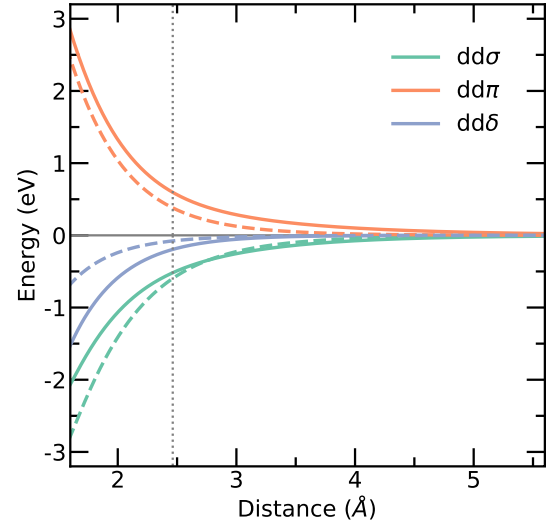


FIG. 1. Bond integrals for Fe-Co as obtained from downfolding the DFT wave function of a dimer onto an orthogonal TB basis [44] (dashed lines) and after our BOP optimization (solid lines) as a function of distance. A dotted gray line indicates the first-nearest-neighbor distance in ferromagnetic (FM) B2 FeCo.

B. Fitting

We constructed the BOP for the Fe-Co in two stages. At first, using unary reference data, we parameterized the Fe-Fe and Co-Co interactions. Then we fixed these elemental interactions and parameterized the Fe-Co interaction with binary reference data. We fit the parameters of the Fe-Fe, Co-Co, and Fe-Co interactions to the corresponding E-V curves using the least-squares method, with higher weights for the most stable phases of Fe, Co, and Fe-Co. We optimized the parameters of our model with the BOPcat software package [56] using the Levenberg-Marquardt method [57,58].

We chose initial guesses for the bond integrals [Eq. (5)] for Fe-Fe and Co-Co interactions based on a previous parametrization [59]. For Fe-Co, we took the initial guess as the average of the optimized Fe-Fe and Co-Co bond integrals because the TB bond integrals of the Fe-Co dimer are between those of the Fe-Fe and Co-Co dimers (see discussion in Ref. [44]).

The number of valence electrons and the Stoner exchange integral are continuous parameters in the TB/BOP [26] formalism. We chose the number of valence d electrons as 6.98 for Fe and 8.20 for Co to reproduce the FM bcc and FM hcp as the ground-state structures, respectively. By setting the Stoner exchange integrals to 0.751 eV and 0.841 eV for Fe and Co, we captured energy differences between magnetic and nonmagnetic structures for elemental Fe and Co (see Fig. 2 in Supplemental Material [60]).

We optimized the initial parameters of energy contributions in Eq. (1) to achieve the best agreement with the reference data. The resulting parameters are compiled in Table 1 in the Supplemental Material [60]. Figure 1 shows the optimized bond integrals $dd\sigma$, $dd\pi$, and $dd\delta$ as a function of distance R [see Eq. (5)] for the Fe-Co interaction compared with the bond integrals obtained by projecting the DFT eigenstates of

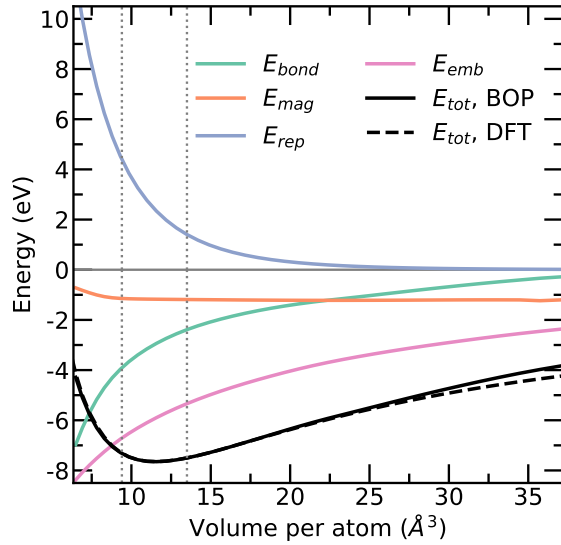


FIG. 2. Contributions to the total binding energy [Eq. (1)] of the parameterized BOP for ferromagnetic (FM) B2 FeCo. The BOP total binding energy curve is compared with corresponding DFT results. The dotted gray lines indicate the range of volumes that we considered in the parametrization.

the Fe-Co dimer onto an orthogonal TB basis [44]. The Fe-Co bond integrals optimized for bulk reference data are close to the bond integrals for the dimer. They differ visually because the surrounding atoms screen the bond between two atoms in a solid [61], which is not the case for a dimer. The resulting bond integrals for the Fe-Fe and Co-Co interactions are shown in Fig. 1 in the Supplemental Material [60]. Figure 2 shows the contributions of the different terms to the total binding energy [Eq. (1)] for FM B2 FeCo for the optimized BOP. The embedding energy E_{emb} that mimics the binding from s electrons and the bond energy E_{bond} from the d electrons are attractive for all volumes and counteracted by the repulsive energy E_{rep} . The magnetic energy E_{mag} delivers a nearly constant energy gain that vanishes at small volumes when the magnetic moment starts to collapse. The core repulsion [Eq. (9)] is short range and not seen in this graph. The total binding energy agrees with DFT results for volumes far beyond those we used as a reference. This is due to the underlying physical model, which leads to high transferability. In the following section we validate the Fe-Co BOP by computing the electronic structure, structural stability, structural transformations, elastic constants, phonons, point and planar defects, and formation energies of Fe-Co alloys. The elemental Fe and Co BOP validation are compiled in the Supplemental Material [60] (see, also, Refs. [62–64] therein). It is worth noting that our Fe BOP shows improvements compared to existing BOP parametrizations [30,32], e.g., for the fcc and hcp structures.

IV. VALIDATION

A. Electronic structure and magnetism of B2 FeCo

The BOP model is based on a coarse-grained description of the electronic structure. Therefore a direct and intuitive

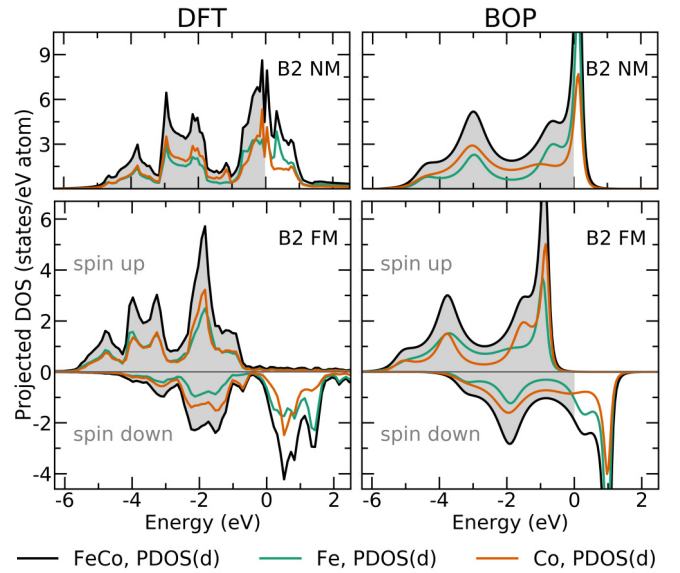


FIG. 3. Electronic DOS of nonmagnetic (NM) and ferromagnetic (FM) B2 FeCo obtained with DFT (left) and BOP (right). For the DFT-DOS, the projection on d orbitals is plotted for consistent comparison with d -valent BOP. The Fermi energy is taken as 0 eV.

test compares the electronic DOS predicted with BOP and the DOS obtained with DFT. In Fig. 3 we compare them for B2 FeCo, the ground-state structure at 1:1 composition, for NM and FM configurations. The DOS is split into the contributions from Fe and Co atoms in both BOP and DFT. For a consistent comparison with our d -valent BOP, we consider only the projection of the DFT-DOS on d orbitals.

The BOP-DOS is well-matched with the DFT-DOS for both NM and FM configurations. It is smoother overall due to the chosen low number of moments (see Sec. II), but it captures the positions and height of the main features and the bandwidth. The BOP captures the peak at the Fermi level for the NM configuration, fulfilling the Stoner criterion and stabilizing the FM B2 phase. It also correctly describes the relative weight of the Fe and Co atoms. In general, an accurate description of the DOS means that the BOP captures the physics of magnetism in the interaction of Fe and Co atoms. We can obtain the BOP-DOS that agrees better with DFT if we use not nine but more moments. However, this will increase the computational cost of calculations. Figure 4 in the Supplemental Material [60] shows an example of the BOP-DOS for FM B2 FeCo computed with 25 moments that reproduces more features of the DFT-DOS.

The electronic DOS of magnetic B2 FeCo obtained with our BOP (Fig. 3) results in magnetic moments of $3.01\mu_B$ for Fe and $1.81\mu_B$ for Co atoms. For elemental bcc Fe and bcc Co, our BOP gives $2.88\mu_B$ and $1.80\mu_B$, respectively. Thus the magnetic moments are almost the same for Co atoms, while they are significantly higher for Fe atoms in the B2 phase compared to elemental bcc. This behavior of the Fe and Co magnetic moments is consistent with DFT calculations. The DFT results in B2 are $2.80\mu_B$ for Fe atoms and $1.81\mu_B$ for Co. For elemental bcc, DFT magnetic moments are $2.24\mu_B$ and $1.82\mu_B$, respectively [65].

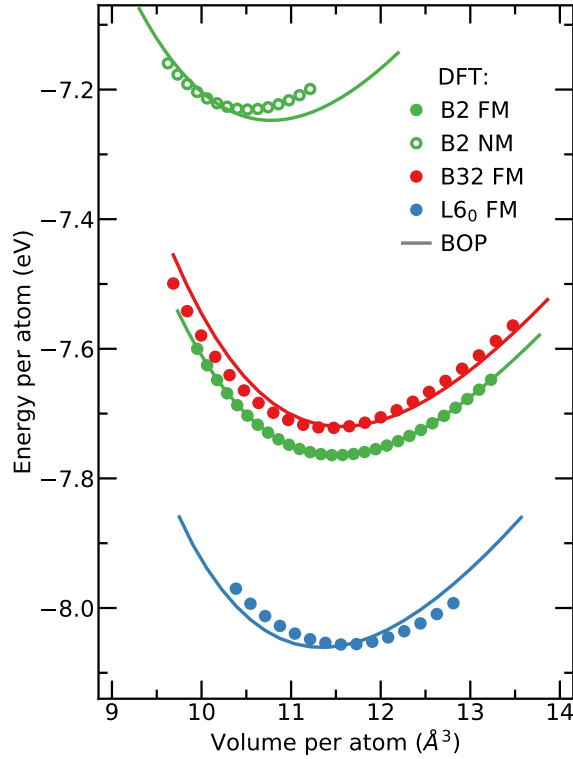


FIG. 4. Comparison of energy-volume (E-V) curves of Fe-Co BOP (lines) and all DFT reference data points we used in the parametrization of Fe-Co interaction (circles).

B. Energy-volume curves of ordered Fe-Co alloys

We further validate the Fe-Co BOP by assessing the total binding energy E_{tot} [Eq. (1)]. Figure 4 compares BOP and DFT E-V curves for the complete set of Fe-Co reference data we used. The BOP perfectly reproduces the DFT E-V curve for FM B2, the most stable phase at 1:1 composition, while the E-V curve of NM B2, which has higher energy, also agrees well, given that we gave it lower weights during fitting. The basis for capturing this energy difference between magnetic and nonmagnetic B2 is the accurate description of the underlying electronic structure, as shown in Fig. 3.

C. Structural stability across chemical compositions

To assess the reliability of the Fe-Co BOP for various chemical compositions, we determined the convex hull of the formation energies at 0 K. The convex hull of the Fe-Co system, in addition to B2, exhibits a dense set of ordered bcc-based stable structures for Fe-rich compositions in regular composition steps of 1/16 [48]. In contrast, all structures on the Co-rich side lie above or close to the tie line connecting B2 and hcp Co.

To compare our BOP with DFT, we computed energies of formation of the Fe-Co binary alloys as

$$E_f = \frac{E(\text{Fe}_x\text{Co}_y) - xE(\text{Fe}) - yE(\text{Co})}{x + y}, \quad (14)$$

where $E(\text{Fe}_x\text{Co}_y)$ is the total energy of a given alloy's supercell, and $E(\text{Fe})$ and $E(\text{Co})$ are total energies per atom of the elemental ground states bcc Fe and hcp Co. The crystal

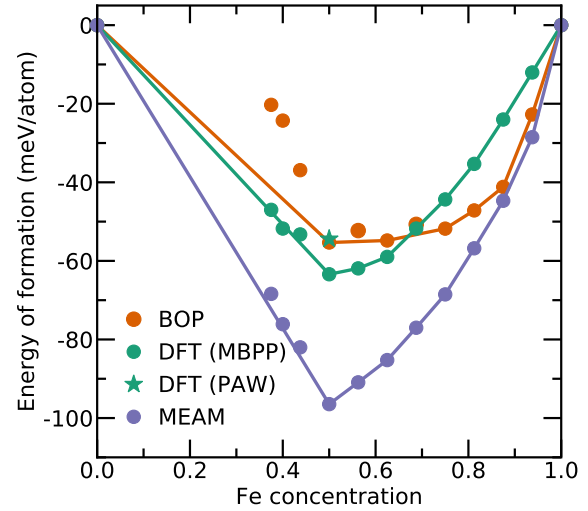


FIG. 5. Energies of formation for ordered bcc-based Fe-Co structures (circles) at various concentrations calculated with BOP, DFT [49], and MEAM [66]. Lines connect the stable structures, forming a convex hull.

structures from the convex hull are given in the Appendix of Ref. [49].

Figure 5 compares the energies of formation calculated with DFT [49], BOP, and modified embedded atom method (MEAM) [66]. The BOP reproduces the dense set of stable structures for Fe-rich compositions with an accuracy of approximately 10 meV/atom. The Fe_9Co_7 and $\text{Fe}_{11}\text{Co}_5$ structures are not on the BOP convex hull but close within less than 3 meV, which seems remarkable as only two stable structures, B2 and L6_0 , were included in the reference data. DFT and BOP B2 energies differ because the DFT data was obtained with the mixed-basis pseudopotential (MBPP) method, whereas we fitted the BOP to DFT obtained with PAW (cf. Table II in Ref. [49]). The difference between MEAM and DFT is significant and may be due to the choice of reference data in the construction of the MEAM.

D. Structural stability of disordered Fe-Co alloys

Fe-Co at 1:1 composition transforms from ordered B2 to disordered bcc (A2) at around 1000 K and further to disordered fcc (A1) above 1200 K [47]. To assess whether our BOP may reproduce these phase transitions, we determined the relative stability of A1, A2, and B2 at 1:1 composition at 0 K as a precursor for predicting the phase transitions [67]. We considered FM and NM configurations as the A2-A1 transition temperature coincides with the Curie temperature. We represented the bcc and fcc solid solutions by special quasirandom structures (SQS) [68] with 16-atom cells from Refs. [69] and [70], respectively.

The comparison to DFT (and also MEAM) results in Fig. 6 shows that the BOP accurately predicts the sequence of structural stability from ordered B2-FM to disordered A2-FM to disordered A1-FM. It also predicts the correct sequence for the energetically higher NM configurations with the most significant deviation for A2-NM. Thus we see that BOP has strong predictive power for disordered phases that were not

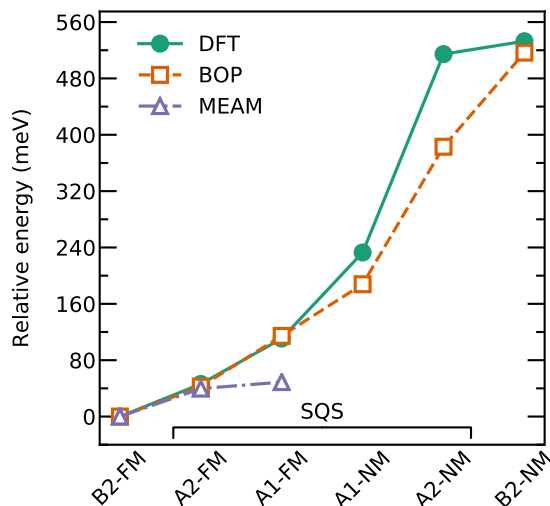


FIG. 6. Structural stability of B2, disordered bcc (A2), and fcc (A1) phases in ferromagnetic (FM) and nonmagnetic (NM) configurations relative to FM B2 computed with BOP, DFT, and MEAM.

part of the reference data. Our results also confirm the conclusions of Abrikosov *et al.* [8], made with DFT using coherent potential approximation (CPA), that magnetism is crucial for stabilizing B2 relative to disordered phases. We should note that the MEAM results in Fig. 6 are given only for the FM configuration, as it was fitted to FM reference data, and magnetism is not included in this potential explicitly.

E. Elastic constants of B2 FeCo

To test the mechanical properties, we compared the bulk modulus (B), elastic constants (C_{11} , C_{12} , C_{44}), and tetragonal shear constant (C') computed with BOP to values calculated with DFT, the embedded atom method (EAM) [71], and modified EAM (MEAM) [72–74] potentials, as well as available experimental data (see Table I). The BOP values for bulk modulus, C_{11} , C_{12} , and C' elastic constants, agree with the DFT results. BOP underestimates C_{44} due to the absence of sheared Fe-Co structures in the reference data.

F. Phonon spectrum of B2 FeCo

Existing TB/BOP models for Fe [30–32] have captured magnetic [33] and structural [34] phase transitions at finite temperatures. Interatomic potential should accurately describe lattice vibrations to achieve transferability beyond the 0 K reference data. In Fig. 7 we compare the phonon DOS of FM B2 FeCo calculated with BOP, DFT, and MEAM [66]. We used the PHONOPY package to compute the phonon DOS [81]. BOP reproduces the main features of the DOS with two prominent peaks and an intermediate peak in between, while the MEAM produces a different shape. Our BOP slightly underestimates the frequency width of the DOS, but overall the BOP predictions are convincing, given that the reference data did not include forces.

TABLE I. Bulk modulus and elastic constants for ferromagnetic (FM) B2 FeCo obtained using BOP, DFT, experiment, and empirical interatomic potentials. All values are in GPa.

	B	C_{11}	C_{12}	C_{44}	C'
BOP ^a	190	268	153	85	58
DFT ^a	191	271	155	128	58
DFT ^b	188	263	152	108	56
DFT ^c	189	259	154	131	53
MEAM ^d	196	268	179	138	27
EAM ^e	187	226	168	136	29
MEAM ^f	188	261	151	127	55
Exp.	188 ^g				61 ^h

^aThis work.

^bReference [75].

^cReference [76].

^dReference [66].

^eReference [77].

^fReference [78].

^gReference [79], measured at 300 K.

^hReference [80], measured at 61 K.

G. Point defects in B2 FeCo

Point defects play a crucial role in Fe-Co and largely determine the stability of the ordered B2 phase [9]. For this reason we calculated the formation energies of vacancies and antisite defects for B2 with a 1:1 composition at 0 K with our BOP. We computed approximate formation energies following derivations of Meyer and Fähnle for antistructure-type systems (Eq. (A7) in Ref. [82]). They assumed that for such systems, the formation energies of antisites of different species are equal. In the Supplemental Material [60] (see, also, Refs. [83,84] therein), we calculated the formation energies differently and confirmed that our BOP predicts the assumed antistructure type of B2 FeCo. Figure 8 compares the formation energies of vacancies and antisite defects obtained using BOP, DFT [9,85], and MEAM [66]. Even though the BOP

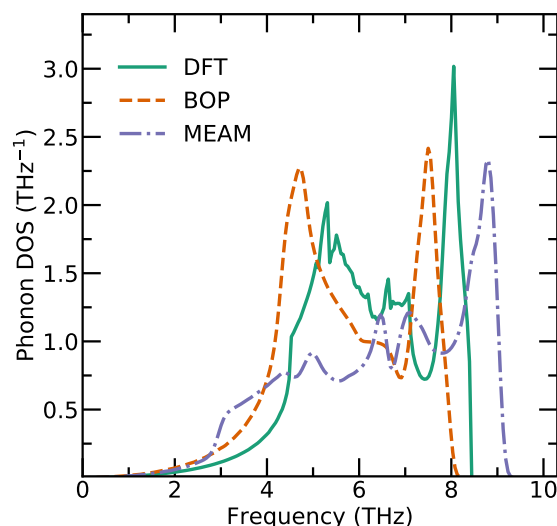


FIG. 7. Phonon DOS of ferromagnetic (FM) B2 FeCo obtained using DFT, BOP, and MEAM [66].

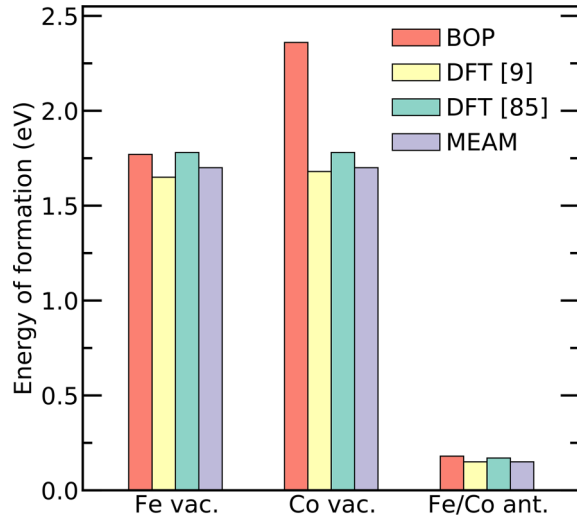


FIG. 8. Defect formation energies for Fe and Co vacancies and antisites in ferromagnetic (FM) B2 FeCo at 1:1 composition at 0 K computed using BOP, DFT [9,85], and MEAM [66]. The formation energies of Fe and Co antisites are the same (according to Eq. (A7) in Ref. [82]; see details in Sec. IV G).

value for a Co vacancy is slightly higher than the DFT, overall, BOP correctly predicts that the formation energies of vacancies are much higher than of antisite defects, making the latter the dominant defects in B2 FeCo. The small but still positive formation energy of antisite defects prevents the spontaneous exchange of Fe and Co atoms and hence stabilizes the B2 phase relative to disordered bcc. The formation energies of defects were not part of the reference data for our BOP, and their correct reproduction demonstrates the transferability of the potential.

H. B2-L1₀ transformation path

DFT predicts that the tetragonal distortion by increasing the c/a ratio of the lattice parameters of B2 FeCo will produce magnetic properties desirable for storage devices: high magnetic saturation moment and giant magnetic anisotropy [86]. Such a distortion is feasible in practice, for example, in L1₀ FeCo, which can be grown as a thin film on Cu substrates [87]. For this reason and to validate our BOP against atomic environments that differ from bcc, we computed the transformation path from bcc-based B2 to fcc-based L1₀ by continuous variation of the c/a ratio. The results of BOP, DFT, and MEAM [66] for FM and NM (not applicable for MEAM; see Sec. IV D) configurations are compiled in Fig. 9 using the standard Bain path notation, with $c/a = 1$ for B2 and $c/a = 1.41$ for L1₀. Overall the BOP precisely reproduces the DFT transformation path for both FM and NM configurations. The agreement for the NM case is particularly striking, because even the only reference structure along the transition path, B2, had a low weight during the fitting. This finding highlights the predictive power of the Fe-Co BOP to atomic environments beyond the reference data that included only structures with $c/a = 1$.

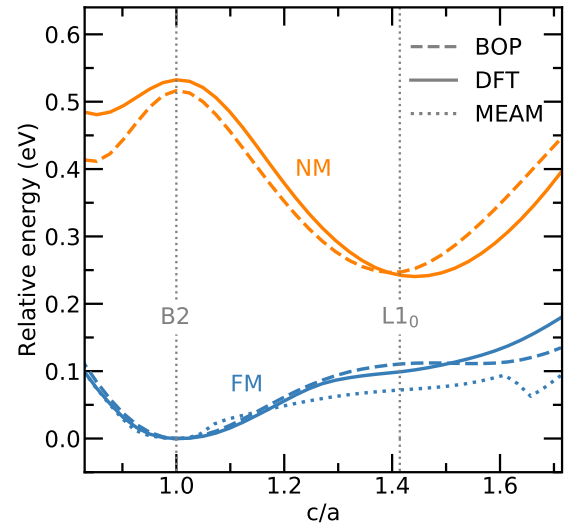


FIG. 9. Transformation path from bcc-based B2 to fcc-based L1₀ phase for ferromagnetic (FM) and nonmagnetic (NM) configurations obtained with BOP, DFT, and MEAM [66].

I. Grain-boundary energies

To test atomic environments with bond angles and nearest-neighbor coordination different from ideal crystal structures, we investigated three typical grain boundaries (GBs) in B2 FeCo. We considered the $\Sigma 5001$ and $\Sigma 3011$ twist GBs as well as the $\Sigma 3[011](1-11)$ tilt GB with rotation angles of 36.87° , 70.53° , and 70.53° , respectively. We constructed the corresponding supercells with 120, 144, and 72 atoms and six B2 unit-cell distances between two adjacent GB planes with the AIMSGB package [88]. We computed the GB energy, γ_{GB} , by DFT, BOP, and MEAM with complete

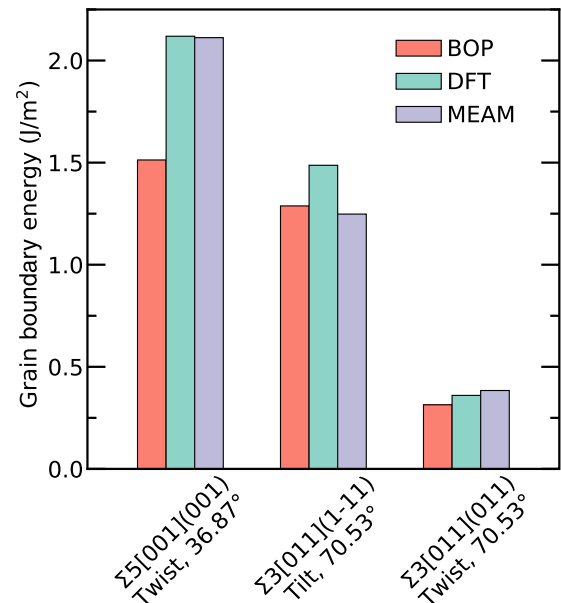


FIG. 10. Energies of two twist and one tilt grain boundaries (GBs) in the ferromagnetic (FM) B2 phase computed using BOP, DFT, and MEAM [66].

relaxation of atomic positions as

$$\gamma_{\text{GB}} = \frac{E_{\text{GB}} - E_{\text{bulk}}}{2A_{\text{GB}}}, \quad (15)$$

where E_{GB} is the energy of a supercell with GB of area A_{GB} and E_{bulk} is the energy of a bulk supercell with the same number of atoms.

The comparison in Fig. 10 shows that MEAM [66] and BOP reproduce the energetic ordering of the GBs. BOP accurately captures the energies of the $\Sigma 3$ -twist and the $\Sigma 3$ -tilt GBs while slightly underestimating the $\Sigma 5$ -twist GB. As we see, our BOP shows considerable transferability to complex atomic environments such as GBs.

V. CONCLUSIONS

We developed an analytic bond-order potential for Fe-Co alloys that includes an explicit treatment of magnetism. We use a d -valent orthogonal tight-binding Hamiltonian in two-center approximation and employ an embedding function to account for the s electrons. The functional form is physically transparent and, for this reason, requires only a small set of reference data. At the same time, the underlying physics ensures robust predictions of Fe-Co properties that we did not include in the fit. We demonstrate the transferability of our

potential to various material properties: structural stability of ordered and disordered phases, elastic constants and phonons, point defects, structural transformations, and planar defects. Due to the explicit treatment of magnetism, our BOP reproduces the main features of the DFT electronic structure for magnetic and nonmagnetic phases. Further, the BOP reproduces the dense sequence of stable phases for Fe-rich Fe-Co alloys with an accuracy of about 10 meV to DFT results and the B2 stability against disordered phases provided by magnetism. The analytic BOP for Fe-Co paves the way to atomistic simulations of Fe-Co alloys with a reliable treatment of magnetism at length- and timescales inaccessible with DFT.

ACKNOWLEDGMENTS

We acknowledge financial support from the International Max-Planck Research School SurMat and the Wilhelm and Günter Esser Foundation. Part of this work was supported by the German Research Foundation (DFG) through project C1 of the Collaborative Research Center SFB/TR 103 (190389738) as well as by the DFG and the French National Research Agency within the DFG-ANR project Magnetism in iron alloys thermodynamics, kinetics and defects (316673557). We acknowledge Yury Lysogorskiy for technical support and Isabel Pietka for carefully reading the manuscript.

-
- [1] P. Weiss, The magnetic properties of the alloys of the ferromagnetic metals: Iron-nickel, nickel-cobalt, cobalt-iron, *Trans. Faraday Soc.* **8**, 149 (1912).
 - [2] P. Weiss and R. Forrer, La saturation absolue des ferromagnétiques et les lois d'approche en fonction du champ et de la température, *Ann. Phys.* **10**, 279 (1929).
 - [3] J. C. Slater, The ferromagnetism of nickel, II. Temperature effects, *Phys. Rev.* **49**, 931 (1936).
 - [4] L. Pauling, The nature of the interatomic forces in metals, *Phys. Rev.* **54**, 899 (1938).
 - [5] R. S. Sundar and S. C. Deevi, Soft magnetic FeCo alloys: Alloy development, processing, and properties, *Int. Mat. Rev.* **50**, 157 (2005).
 - [6] J. Orehtsky and K. Schroder, Order-disorder critical phenomena in FeCo, *J. Phys. F: Met. Phys.* **4**, 196 (1974).
 - [7] E. Josso, Iron-cobalt-vanadium alloys: A critical study of the phase diagrams in relation to magnetic properties, *IEEE Trans. Magn.* **10**, 161 (1974).
 - [8] I. A. Abrikosov, P. James, O. Eriksson, P. Söderlind, A. V. Ruban, H. L. Skriver, and B. Johansson, Magnetically induced crystal structure and phase stability in $\text{Fe}_{1-c}\text{Co}_c$, *Phys. Rev. B* **54**, 3380 (1996).
 - [9] M. Neumayer and M. Fähnle, Atomic defects in FeCo: Stabilization of the B2 structure by magnetism, *Phys. Rev. B* **64**, 132102 (2001).
 - [10] D. Terentyev, E. Zhurkin, and G. Bonny, Emission of full and partial dislocations from a crack in bcc and fcc metals: An atomistic study, *Comput. Mater. Sci.* **55**, 313 (2012).
 - [11] R. Hadian, B. Grabowski, C. P. Race, and J. Neugebauer, Atomistic migration mechanisms of atomically flat, stepped, and kinked grain boundaries, *Phys. Rev. B* **94**, 165413 (2016).
 - [12] O. A. Restrepo, N. Mousseau, M. Trochet, F. El-Mellouhi, O. Bouhali, and C. S. Becquart, Carbon diffusion paths and segregation at high-angle tilt grain boundaries in α -Fe studied by using a kinetic activation-relation technique, *Phys. Rev. B* **97**, 054309 (2018).
 - [13] C. P. Race, R. Hadian, J. von Pezold, B. Grabowski, and J. Neugebauer, Mechanisms and kinetics of the migration of grain boundaries containing extended defects, *Phys. Rev. B* **92**, 174115 (2015).
 - [14] F. Maresca, D. Dragoni, G. Csányi, N. Marzari, and W. A. Curtin, Screw dislocation structure and mobility in body centered cubic Fe predicted by a Gaussian approximation potential, *npj Comput. Mater.* **4**, 69 (2018).
 - [15] G. Singh, J. R. Kermode, A. De Vita, and R. W. Zimmerman, Validity of linear elasticity in the crack-tip region of ideal brittle solids, *Int. J. Fract.* **189**, 103 (2014).
 - [16] L. Romaner, V. I. Razumovskiy, and R. Pippan, Core polarity of screw dislocations in Fe-Co alloys, *Philos. Mag. Lett.* **94**, 334 (2014).
 - [17] M. R. Gilbert and S. L. Dudarev, Ab initio multi-string Frenkel-Kontorova model for a $b = a/2[111]$ screw dislocation in bcc iron, *Philos. Mag.* **90**, 1035 (2010).
 - [18] V. L. Deringer, M. A. Caro, and G. Csányi, Machine learning interatomic potentials as emerging tools for materials science, *Adv. Mater.* **31**, 1902765 (2019).
 - [19] Y. Mishin, Machine-learning interatomic potentials for materials science, *Acta Mater.* **214**, 116980 (2021).
 - [20] H. Kulik, T. Hammerschmidt, J. Schmidt, S. Botti, M. Marques, M. Boley, M. Scheffler, M. Todorović, P. Rinke, C. Oses *et al.*, Roadmap on machine learning in electronic structure, *Electron. Struct.* **4**, 023004 (2022).

- [21] R. Freitas and Y. Cao, Machine-learning potentials for crystal defects, *MRS Commun.* **12**, 510 (2022).
- [22] M. Eckhoff and J. Behler, High-dimensional neural network potentials for magnetic systems using spin-dependent atom-centered symmetry functions, *npj Comput. Mater.* **7**, 170 (2021).
- [23] R. Drautz, Atomic cluster expansion of scalar, vectorial, and tensorial properties including magnetism and charge transfer, *Phys. Rev. B* **102**, 024104 (2020).
- [24] I. Novikov, B. Grabowski, F. Körmann, and A. Shapeev, Magnetic moment tensor potentials for collinear spin-polarized materials reproduce different magnetic states of bcc Fe, *npj Comput. Mater.* **8**, 13 (2022).
- [25] R. Drautz and D. G. Pettifor, Valence-dependent analytic bond-order potential for transition metals, *Phys. Rev. B* **74**, 174117 (2006).
- [26] R. Drautz and D. G. Pettifor, Valence-dependent analytic bond-order potential for magnetic transition metals, *Phys. Rev. B* **84**, 214114 (2011).
- [27] M. Čák, T. Hammerschmidt, J. Rogal, V. Vitek, and R. Drautz, Analytic bond-order potentials for the bcc refractory metals Nb, Ta, Mo, and W, *J. Phys.: Condens. Matter* **26**, 195501 (2014).
- [28] A. Ferrari, M. Schröder, Y. Lysogorskiy, J. Rogal, M. Mrovec, and R. Drautz, Phase transitions in titanium with an analytic bond-order potential, *Modell. Simul. Mater. Sci. Eng.* **27**, 085008 (2019).
- [29] J. F. Drain, R. Drautz, and D. G. Pettifor, Magnetic analytic bond-order potential for modeling the different phases of Mn at zero kelvin, *Phys. Rev. B* **89**, 134102 (2014).
- [30] M. Mrovec, D. Nguyen-Manh, C. Elsässer, and P. Gumbsch, Magnetic Bond-Order Potential for Iron, *Phys. Rev. Lett.* **106**, 246402 (2011).
- [31] G. K. H. Madsen, E. J. McEniry, and R. Drautz, Optimized orthogonal tight-binding basis: Application to iron, *Phys. Rev. B* **83**, 184119 (2011).
- [32] M. Ford, R. Drautz, T. Hammerschmidt, and D. G. Pettifor, Convergence of an analytic bond-order potential for collinear magnetism in Fe, *Modell. Simul. Mater. Sci. Eng.* **22**, 034005 (2014).
- [33] N. Wang, T. Hammerschmidt, J. Rogal, and R. Drautz, Accelerating spin-space sampling by auxiliary spin dynamics and temperature-dependent spin-cluster expansion, *Phys. Rev. B* **99**, 094402 (2019).
- [34] N. Wang, T. Hammerschmidt, T. Hickel, J. Rogal, and R. Drautz, Influence of spin fluctuations on structural phase transitions of iron, *Phys. Rev. B* **107**, 104108 (2023).
- [35] C. Teijeiro, T. Hammerschmidt, R. Drautz, and G. Sutmann, Efficient parallelization of analytic bond-order potentials for large-scale atomistic simulations, *Comput. Phys. Commun.* **204**, 64 (2016).
- [36] C. Teijeiro, T. Hammerschmidt, R. Drautz, and G. Sutmann, Optimized parallel simulations of analytic bond-order potentials on hybrid shared/distributed memory with mpi and openmp, *Int. J. High Perform. Comput. Appl.* **33**, 227 (2019).
- [37] A. P. Sutton, M. W. Finnis, D. G. Pettifor, and Y. Ohta, The tight-binding bond model, *J. Phys. C: Solid State Phys.* **21**, 35 (1988).
- [38] R. Drautz, T. Hammerschmidt, M. Cak, and D. G. Pettifor, Bond-order potentials: Derivation and parameterization for refractory elements, *Modell. Simul. Mater. Sci. Eng.* **23**, 074004 (2015).
- [39] T. Hammerschmidt, B. Seiser, M. Ford, A. Ladines, S. Schreiber, N. Wang, J. Jenke, Y. Lysogorskiy, C. Teijeiro, M. Mrovec, M. Cak, E. Margine, D. Pettifor, and R. Drautz, BOPfox program for tight-binding and analytic bond-order potential calculations, *Comput. Phys. Commun.* **235**, 221 (2019).
- [40] F. Cyrot-Lackmann, On the electronic structure of liquid transitional metals, *Adv. Phys.* **16**, 393 (1967).
- [41] T. Hammerschmidt and R. Drautz, Bond-order potentials for bridging the electronic to atomistic modelling hierarchies, in *Multiscale Simulations Methods in Molecular Sciences*, edited by J. Grotendorst, N. Attig, S. Blugel, and D. Marx (John von Neumann Institute for Computing, Jülich, 2009), Vol. 42, pp. 229–246.
- [42] B. Seiser, D. G. Pettifor, and R. Drautz, Analytic bond-order potential expansion of recursion-based methods, *Phys. Rev. B* **87**, 094105 (2013).
- [43] M. J. Cawkwell, D. Nguyen-Manh, D. G. Pettifor, and V. Vitek, Construction, assessment and application of bond-order potential for iridium, *Phys. Rev. B* **73**, 064104 (2006).
- [44] J. Jenke, A. N. Ladines, T. Hammerschmidt, D. G. Pettifor, and R. Drautz, Tight-binding bond parameters for dimers across the periodic table from density-functional theory, *Phys. Rev. Mater.* **5**, 023801 (2021).
- [45] E. Stoner, Collective electron ferromagnetism II. Energy and specific heat, *Proc. R. Soc. A* **169**, 339 (1939).
- [46] S. Znam, D. Nguyen-Manh, D. G. Pettifor, and V. Vitek, Atomistic modelling of TiAl: I. Bond-order potentials with environmental dependence, *Philos. Mag.* **83**, 415 (2003).
- [47] O. von Goldbeck, Iron-cobalt Fe-Co, in *IRON-Binary Phase Diagrams* (Springer, Berlin, Heidelberg, 1982), pp. 27–31.
- [48] R. Drautz, A. Díaz-Ortiz, M. Fähnle, and H. Dosch, Ordering and Magnetism in Fe-Co: Dense Sequence of Ground-State Structures, *Phys. Rev. Lett.* **93**, 067202 (2004).
- [49] A. Díaz-Ortiz, R. Drautz, M. Fähnle, H. Dosch, and J. M. Sanchez, Structure and magnetism in bcc-based iron-cobalt alloys, *Phys. Rev. B* **73**, 224208 (2006).
- [50] G. Kresse and J. Hafner, Ab initio molecular dynamics for liquid metals, *Phys. Rev. B* **47**, 558 (1993).
- [51] G. Kresse and J. Hafner, Ab initio molecular-dynamics simulation of the liquid-metal–amorphous-semiconductor transition in germanium, *Phys. Rev. B* **49**, 14251 (1994).
- [52] G. Kresse and J. Furthmüller, Efficiency of ab-initio total energy calculations for metals and semiconductors using a plane-wave basis set, *Comput. Mater. Sci.* **6**, 15 (1996).
- [53] G. Kresse and D. Joubert, From ultrasoft pseudopotentials to the projector augmented-wave method, *Phys. Rev. B* **59**, 1758 (1999).
- [54] J. P. Perdew, K. Burke, and M. Ernzerhof, Generalized Gradient Approximation Made Simple, *Phys. Rev. Lett.* **77**, 3865 (1996).
- [55] H. J. Monkhorst and J. D. Pack, Special points for Brillouin-zone integrations, *Phys. Rev. B* **13**, 5188 (1976).
- [56] A. Ladines, T. Hammerschmidt, and R. Drautz, BOPcat software package for the construction and testing of tight-binding models and bond-order potentials, *Comput. Mater. Sci.* **173**, 109455 (2020).
- [57] K. Levenberg, A method for the solution of certain non-linear problems in least squares, *Quart. Appl. Math.* **2**, 164 (1944).

- [58] D. W. Marquardt, An algorithm for least-squares estimation of nonlinear parameters, *J. Soc. Ind. Appl. Math.* **11**, 431 (1963).
- [59] A. P. A. Subramanyam, Ph.D. thesis, Ruhr-Universität Bochum, Germany, 2022.
- [60] See Supplemental Material at <http://link.aps.org/supplemental/10.1103/PhysRevMaterials.7.044403> for details of the BOP model, tests of Fe and Co sub-models, B2 FeCo electronic DOS obtained with 25 moments, and discussion of defect formation energies calculations.
- [61] D. Nguyen-Manh, D. G. Pettifor, and V. Vitek, Analytic Environment-Dependent Tight-Binding Bond Integrals: Application to MoSi₂, *Phys. Rev. Lett.* **85**, 4136 (2000).
- [62] R. Lizárraga, F. Pan, L. Bergqvist, E. Holmström, Z. Gercsi, and L. Vitos, First principles theory of the hcp-fcc phase transition in cobalt, *Sci. Rep.* **7**, 3778 (2017).
- [63] X. Sha and R. E. Cohen, Lattice dynamics and thermodynamics of bcc iron under pressure: First-principles linear response study, *Phys. Rev. B* **73**, 104303 (2006).
- [64] B. Medasani, M. Haranczyk, A. Canning, and M. Asta, Vacancy formation energies in metals: A comparison of MetaGGA with LDA and GGA exchange-correlation functionals, *Comput. Mater. Sci.* **101**, 96 (2015).
- [65] C. Park, I. Kim, B. Lee, and J. Lee, Origin of the magnetic moment enhancement of the ordered Fe₅₀Co₅₀ alloys, *Phys. Status Solidi B* **241**, 1419 (2004).
- [66] W.-M. Choi, Y. Kim, D. Seol, and B.-J. Lee, Modified embedded-atom method interatomic potentials for the Co-Cr, Co-Fe, Co-Mn, Cr-Mn and Mn-Ni binary systems, *Comput. Mater. Sci.* **130**, 121 (2017).
- [67] T. Chakraborty, J. Rogal, and R. Drautz, Unraveling the composition dependence of the martensitic transformation temperature: A first-principles study of Ti-Ta alloys, *Phys. Rev. B* **94**, 224104 (2016).
- [68] A. Zunger, S.-H. Wei, L. G. Ferreira, and J. E. Bernard, Special Quasirandom Structures, *Phys. Rev. Lett.* **65**, 353 (1990).
- [69] C. Jiang, C. Wolverton, J. Sofo, L.-Q. Chen, and Z.-K. Liu, First-principles study of binary bcc alloys using special quasirandom structures, *Phys. Rev. B* **69**, 214202 (2004).
- [70] C. Wolverton, Crystal structure and stability of complex precipitate phases in Al-Cu-Mg-(Si) and Al-Zn-Mg alloys, *Acta Mater.* **49**, 3129 (2001).
- [71] M. S. Daw and M. I. Baskes, Embedded-atom method: Derivation and application to impurities, surfaces, and other defects in metals, *Phys. Rev. B* **29**, 6443 (1984).
- [72] M. I. Baskes, Modified embedded-atom potentials for cubic materials and impurities, *Phys. Rev. B* **46**, 2727 (1992).
- [73] B.-J. Lee and M. I. Baskes, Second nearest-neighbor modified embedded-atom-method potential, *Phys. Rev. B* **62**, 8564 (2000).
- [74] B.-J. Lee, M. I. Baskes, H. Kim, and Y. K. Cho, Second nearest-neighbor modified embedded atom method potentials for bcc transition metals, *Phys. Rev. B* **64**, 184102 (2001).
- [75] M. Rahaman, Ph.D. thesis, KTH Royal Institute of Technology, Sweden, 2013.
- [76] A. Jain, S. P. Ong, G. Hautier, W. Chen, W. D. Richards, S. Dacek, S. Cholia, D. Gunter, D. Skinner, G. Ceder, and K. A. Persson, The Materials Project: A materials genome approach to accelerating materials innovation, *APL Mater.* **1**, 011002 (2013).
- [77] Y. Li, X. Cheng, W. Duan, and W. Qiang, Improved ductility by coupled motion of grain boundaries in nanocrystalline B2-FeCo alloys, *Comput. Mater. Sci.* **198**, 110703 (2021).
- [78] M. Muralles, J. T. Oh, and Z. Chen, Molecular dynamics study of FeCo phase transitions and thermal properties based on an improved 2NN MEAM potential, *J. Mat. Res. Tech.* **19**, 1102 (2022).
- [79] O. Belousov and N. Palii, Concentration and temperature dependences of the elastic properties of quenched Fe-Co and FeCo-2V alloys, *Russ. Metall.* **2009**, 41 (2009).
- [80] A. Clark, J. Restorff, M. Wun-Fogle, D. Wu, and T. A. Lograsso, Temperature dependence of the magnetostriction and magnetoelastic coupling in Fe_{100-x}Al_x (x= 14.1, 16.6, 21.5, 26.3) and Fe₅₀Co₅₀, *J. Appl. Phys.* **103**, 07B310 (2008).
- [81] A. Togo and I. Tanaka, First principles phonon calculations in materials science, *Scripta Mater.* **108**, 1 (2015).
- [82] B. Meyer and M. Fähnle, Atomic defects in the ordered compound B2-NiAl: A combination of ab initio electron theory and statistical mechanics, *Phys. Rev. B* **59**, 6072 (1999).
- [83] G.-X. Qian, R. M. Martin, and D. J. Chadi, First-principles study of the atomic reconstructions and energies of Ga- and As-stabilized GaAs(100) surfaces, *Phys. Rev. B* **38**, 7649 (1988).
- [84] S. B. Zhang and J. E. Northrup, Chemical Potential Dependence of Defect Formation Energies in GaAs: Application to Ga Self-Diffusion, *Phys. Rev. Lett.* **67**, 2339 (1991).
- [85] C. L. Fu and M. Krcmar, First-principles study of the structural, defect, and mechanical properties of B2 FeCo alloys, *Phys. Rev. B* **74**, 174108 (2006).
- [86] T. Burkert, L. Nordström, O. Eriksson, and O. Heinonen, Giant Magnetic Anisotropy in Tetragonal FeCo Alloys, *Phys. Rev. Lett.* **93**, 027203 (2004).
- [87] G. A. Farnan, C. L. Fu, Z. Gai, M. Krcmar, A. P. Baddorf, Z. Zhang, and J. Shen, Electronic Stability of Magnetic Fe/Co Superlattices with Monatomic Layer Alternation, *Phys. Rev. Lett.* **91**, 226106 (2003).
- [88] J. Cheng, J. Luo, and K. Yang, Aimgb: An algorithm and open-source python library to generate periodic grain boundary structures, *Comput. Mater. Sci.* **155**, 92 (2018).